Heliyon 9 (2023) e18690

Contents lists available at ScienceDirect

Heliyon

journal homepage: www.cell.com/heliyon

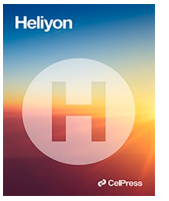

Elucidating the adsorption of 2-Mercaptopyridine drug on the aluminum phosphide ($Al_{12}P_{12}$) nanocage: A DFT study

Al-shimaa S.M. Rady [a], Nayra A.M. Moussa [a], Lamiaa A. Mohamed [a], Peter A. Sidhom [b], Shaban R.M. Sayed [c], Mohamed K. Abd El-Rahman [d], Eslam Dabbish [e], Tamer Shoeib [e,**], Mahmoud A.A. Ibrahim [a,f,*]

[a] Computational Chemistry Laboratory, Chemistry Department, Faculty of Science, Minia University, Minia, 61519, Egypt
[b] Department of Pharmaceutical Chemistry, Faculty of Pharmacy, Tanta University, Tanta, 31527, Egypt
[c] Department of Botany and Microbiology, College of Science, King Saud University, P.O. Box 2455, Riyadh, 11451, Saudi Arabia
[d] Department of Chemistry and Chemical Biology, Harvard University, 12 Oxford Street, Cambridge, MA, 02138, USA
[e] Department of Chemistry, The American University in Cairo, New Cairo, 11835, Egypt
[f] School of Health Sciences, University of KwaZulu-Natal, Westville Campus, Durban, 4000, South Africa

ARTICLE INFO

Keywords:
Mercaptopyridine
Aluminum phosphide nanocage
DFT calculations
SAPT
Thermodynamic parameters

ABSTRACT

Adsorption amplitude of the aluminum phosphide ($Al_{12}P_{12}$) nanocage toward the 2-Mercaptopyridine (MCP) drug was herein monitored based on density functional theory (DFT) calculations. The adsorption process through MCP···$Al_{12}P_{12}$ complex in various configurations was elucidated by means of adsorption (E_{ads}) energies. According to the energetic affirmations, the $Al_{12}P_{12}$ nanocage demonstrated potential versatility toward adsorbing the MCP drug within the investigated configurations and exhibited significant negative adsorption energies up to −27.71 kcal/mol. Upon the results of SAPT analysis, the electrostatic forces showed the highest contributions to the overall adsorption process with energetic values up to −74.36 kcal/mol. Concurrently, variations of molecular orbitals distribution along with alterations in the energy gap (E_{gap}) and Fermi level (E_{FL}) of the studied nanocage were denoted after adsorbing the MCP drug. The favorable impact of water solvent within the MCP···$Al_{12}P_{12}$ complexes was unveiled and confirmed by negative solvation energy (ΔE_{solv}) values up to −17.75 kcal/mol. According to thermodynamic parameters, the spontaneous and exothermic natures of the considered adsorption process were proclaimed by negative values of ΔG and ΔH parameters. Significant changes in the IR and Raman peaks, along with the appearance of new peaks, were noticed, confirming the occurrence of the targeted adsorption process. Furthermore, the adsorption features of the MCP drug on the $Al_{12}N_{12}$ nanocage were elucidated and compared to the $Al_{12}P_{12}$ analog. The obtained results demonstrated the higher preferability of $Al_{12}P_{12}$ nanocage than the $Al_{12}N_{12}$ candidate towards adsorbing the MCP drug without structural distortion.

* Corresponding author. Computational Chemistry Laboratory, Chemistry Department, Faculty of Science, Minia University, Minia 61519, Egypt.
** Corresponding author.
E-mail addresses: t.shoeib@aucegypt.edu (T. Shoeib), m.ibrahim@compchem.net (M.A.A. Ibrahim).

https://doi.org/10.1016/j.heliyon.2023.e18690
Received 11 May 2023; Received in revised form 21 July 2023; Accepted 25 July 2023
Available online 26 July 2023

1. Introduction

Nanoscale materials have become a technological approach with great potential to be applied in various life aspects [1,2] owing to their exceptional properties. In the vast field of nanomaterials, a wide range of structures, including nanocones [3,4], nanotubes [5,6], fullerenes [7,8], and fullerene-like [9–13], has been utilized for drug adsorption and biosensor applications [14,15]. The adsorption of drug molecules over the exterior surface of fullerene-like structures has a vital role in reducing drug side effects [16]. Along with the growing recognition of fullerene-like structures, nanocages have been considered the most proficient ones, addressed by their promising physical and chemical properties.

Within continuing to evolve, inorganic aluminum phosphide ($Al_{12}P_{12}$) as a fullerene-like nanocage was theoretically studied to elucidate its drug-loading efficiency [17]. From the literature, $Al_{12}P_{12}$ was distinguished by high vibrational frequencies, allowing for observing vibrational progressions in photoelectron spectra [18,19]. As promising sensing material, the tendency of the $Al_{12}P_{12}$ nanocage to combine with the pyrrole molecule was examined through DFT calculations [20]. In the same vein, the application of the $Al_{12}P_{12}$ nanocage as a catalyst for the hydrogen evolution reaction was earlier addressed with an observable favorability [21]. A literature survey also documented the applicability of the $Al_{12}P_{12}$ nanocage as supercapacitors [22] and high-performance nonlinear optical (NLO) materials [23]. Furthermore, the potentiality of the $Al_{12}P_{12}$ nanocage for detecting guanine molecules was unveiled, demonstrating the potential application of $Al_{12}P_{12}$ as a biochemical sensor [24]. As an essential issue, the role of $Al_{12}P_{12}$ nanocage in drug adsorption and biosensor applications was previously addressed, albeit in an insufficient manner, reporting the potentiality of $Al_{12}P_{12}$ nanocage to adsorb sulfamide drug [25], 4-aminopyridine drug [26], and sorbic acid drug [27].

Mercaptopyridine is a thiol compound with C_5H_5NS chemical formula that contains more than one hetero atom (i.e., S and N atoms) [28–30]. Mercaptopyridine derivatives are examples of organosulfur compounds that possess an important role in industry, pharmacology, and biology [31]. By dint of such hetero atoms, Mercaptopyridine derivatives gain the π-acidic nature, which imputes their promising role in coordination chemistry [32]. In particular, the Mercaptopyridine derivatives are found to be effective as their undisputed antimicrobial, antifungal, and alkylation properties [33,34]. Recently, the efficacy of Mercaptopyridine derivatives was confirmed against tRNA synthesis and bacterial growth [35]. In a similar vein, Mercaptopyridine derivatives were introduced with significant anticancer activity [36]. In this regard, enthralling interest was oriented toward inspecting the adsorption process of Mercaptopyridine derivatives over nanomaterials [28,37]. The adsorption behavior of Mercaptopyridine derivatives on the surface of $Be_{12}O_{12}$ and $B_{12}P_{12}$ nanocages was accordingly demonstrated with further illustration for the capability of doping effect on the adsorption process [28,37]. Despite the promising features of aluminum-bearing nanocages, no detailed study unveiled its adsorption amplitude toward Mercaptopyridine derivatives, in particular 2-Mercaptopyridine (MCP) anticancer drug.

In this regard, the current work aimed to unveil the adsorption behavior of 2-Mercaptopyridine (MCP) drug on the surface of the aluminum phosphide ($Al_{12}P_{12}$) nanocage for the first time. A thorough understanding of the adsorption process was obtained by conducting various DFT calculations, including electrostatic potential analysis (ESP), noncovalent interaction (NCI) index, symmetry-adapted perturbation theory (SAPT), and quantum theory of atoms in molecules (QTAIM). Thermodynamic parameters were evaluated to elucidate the nature of the adsorption process. For more implementations, Infrared (IR) and Raman spectra were illustrated for the isolated nanocage along with the investigated complexes. The electronic properties were assessed for the investigated MCP···$Al_{12}P_{12}$ complexes. The effect of water solvent on the adsorption process was also investigated for all the studied complexes. An additional comparative elucidation for the efficiency of $Al_{12}P_{12}$ nanocage with $Al_{12}N_{12}$ analog toward adsorbing the MCP drug was then performed. In that spirit, the optimization and adsorption energy calculations were executed for the MCP···$Al_{12}N_{12}$ complexes and compared to MCP···$Al_{12}P_{12}$ analogs. This work would be an efficient linchpin toward evolving the applications of $Al_{12}P_{12}$ nanocage in drug adsorption and biosensor applications.

2. Computational Methods

Herein, the competence of aluminum phosphide ($Al_{12}P_{12}$) nanocage to adsorb 2-Mercaptopyridine (MCP) drug was studied by M06-2X/6-311+G** density functional methods [38]. Geometry optimization of the MCP···$Al_{12}P_{12}$ complex within several configurations was first executed. Afterward, frequency calculations were implemented to ensure if they were true minima or not. Electrostatic potential (ESP) analysis, relying on the optimized systems, was examined to determine the positive and negative potentials on the molecular surface. Regarding ESP, the molecular electrostatic potential (MEP) maps were analyzed and graphed with 0.002 au electron density envelop value [39]. A comprehensive analysis of the ESP was executed by utilizing the Multiwfn 3.7 software to assess the values of the surface electrostatic potential extrema ($V_{s,min}/V_{s,max}$) [40].

The relative potentiality of the $Al_{12}P_{12}$ nanocage to adsorb the MCP drug was examined based on the adsorption energy (E_{ads}) values. All calculated E_{ads} values were treated with the counterpoise corrected (CC) method to eliminate the basis set superposition error (BSSE), as given by equation (1).

$$E_{ads} = E_{MCP\bullet\bullet\bullet Al_{12}P_{12}} - (E_{MCP} + E_{Al_{12}P_{12}}) + E_{BSSE} \quad (1)$$

In equation (1), the energies of MCP···$Al_{12}P_{12}$ complexes and isolated MCP drug and $Al_{12}P_{12}$ nanocage were represented by $E_{MCP\bullet\bullet\bullet Al_{12}P_{12}}$ and E_{MCP} and $E_{Al_{12}P_{12}}$, respectively. The analysis of symmetry-adapted perturbation theory (SAPT) was executed at the SAPT0 level to unveil the physically meaningful components that controlled the adsorption process using PSI4 package [41]. The total SPAT0 energy (E^{SAPT0}) was assessed as the sum of its main components, namely, electrostatic (E_{elst}), exchange (E_{exch}), induction (E_{ind}), and dispersion (E_{disp}), as illustrated in equations (2)–(6) [42].

$$E^{\mathrm{SAPT0}} = E_{\mathrm{elst}} + E_{\mathrm{exch}} + E_{\mathrm{ind}} + E_{\mathrm{disp}} \tag{2}$$

where:

$$E_{\mathrm{elst}} = E_{\mathrm{elst}}^{(10)} \tag{3}$$

$$E_{\mathrm{exch}} = E_{\mathrm{exch}}^{(10)} \tag{4}$$

$$E_{\mathrm{ind}} = E_{\mathrm{ind,resp}}^{(20)} + E_{\mathrm{exch-ind,resp}}^{(20)} + \delta E_{\mathrm{HF,resp}}^{(2)} \tag{5}$$

$$E_{\mathrm{disp}} = E_{\mathrm{disp}}^{(20)} + E_{\mathrm{exch-disp}}^{(20)} \tag{6}$$

Afterward, quantum theory of atoms in molecules (QTAIM) analysis was applied to all studied configurations. In accordance with QTAIM, the bond paths (BPs) and bond critical points (BCPs) were generated; meanwhile, the topological features were calculated. Further, noncovalent interaction (NCI) index was executed, and 3D NCI plots were generated. Consequently, the 3D NCI plots were visualized according to $(\lambda_2)\rho$ values with a color scale starting from blue (−0.035 au) to red (0.020 au). Within the context of Multiwfn 3.7 software [40], QTAIM and NCI calculations were performed.

Frontier molecular orbitals (FMOs) theory was applied to illustrate the alterations in the electronic characteristics of the nanocage and drug. Following FMOs, the distributions of the highest occupied and the lowest unoccupied molecular orbitals (HOMO and LUMO, respectively) were mapped for isolated systems along with their corresponding complexes. Further, the energies of HOMO and LUMO levels (E_{HOMO} and E_{LUMO}, respectively) were computed before and after the MCP adsorption process. According to E_{HOMO} and E_{LUMO} values, Fermi level (E_{FL}) [43] and energy gap (E_{gap}) [44] were accordingly calculated as given by equations (7) and (8).

$$E_{\mathrm{FL}} = E_{\mathrm{HOMO}} + \frac{E_{\mathrm{LUMO}} - E_{\mathrm{HOMO}}}{2} \tag{7}$$

$$E_{\mathrm{gap}} = E_{\mathrm{LUMO}} - E_{\mathrm{HOMO}} \tag{8}$$

The quantum mechanical descriptors, namely, ionization potential (*IP*), electron affinity (*EA*), chemical potential (μ), global hardness (η), global softness (*S*), electrophilicity index (ω), and work function (Φ) [45], were computed for the MCP and $Al_{12}P_{12}$ molecules as well as their corresponding complexes, as given by equations (9)–(15).

$$IP \approx -E_{\mathrm{HOMO}} \tag{9}$$

$$EA \approx -E_{\mathrm{LUMO}} \tag{10}$$

$$\eta = \frac{E_{\mathrm{LUMO}} - E_{\mathrm{HOMO}}}{2} \tag{11}$$

$$\mu = \frac{E_{\mathrm{LUMO}} + E_{\mathrm{HOMO}}}{2} \tag{12}$$

$$s = \frac{1}{\eta} \tag{13}$$

$$\omega = \frac{\mu^2}{2\eta} \tag{14}$$

$$\Phi = V_{eL(+\infty)} - E_{\mathrm{FL}} \tag{15}$$

The vacuum level electrostatic potential is presented as $V_{\mathrm{el}}(+\infty)$ and is presumed to be nearly zero. Further, the attractive nature of the $Al_{12}P_{12}$ nanocage toward the adsorption of MCP drug was elucidated by means of electrical conductivity as given by equation (16).

$$\sigma\ \alpha\ \mathrm{Exp}\left(\frac{-E_{\mathrm{gap}}}{kT}\right) \tag{16}$$

In equation (16), the electrical conductivity, energy gap, Boltzmann's constant, and temperature are represented by σ, E_{gap}, k, and T, respectively. A further illustration of the impact of the adsorption process on the electronic nature was illustrated by generating total and partial density of states (TDOS and PDOS, respectively) plots using GaussSum software [46]. The effect of water solvent on the adsorption process was established by employing the polarizable continuum model (PCM). For the optimized complexes in the water medium, the adsorption energies ($E_{\mathrm{ads}}^{\mathrm{solvent}}$) were calculated. By means of total energies in water and gas phases, the solvation energy (ΔE_{solv}) of the complex could be computed as explained in equation (17).

$$\Delta E_{\mathrm{solv}} = E_{\mathrm{solvent}} - E_{\mathrm{gas}} \tag{17}$$

In an effort to better estimate the favorability of the considered adsorption process, the thermodynamic parameters were computed by performing frequency calculations. Accordingly, the Gibbs free energy (ΔG), enthalpy (ΔH), and entropy (ΔS) changes were evaluated from equations (18) and (19).

$$\Delta M = M_{\mathrm{MCP}\bullet\bullet\bullet\mathrm{Al_{12}P_{12}}} - (M_{\mathrm{MCP}} + M_{\mathrm{Al_{12}P_{12}}}) + E_{\mathrm{BSSE}} \tag{18}$$

$$\Delta S = -(\Delta G - \Delta H)/\mathrm{T} \tag{19}$$

where the quantity of ΔG and ΔH are presented as ΔM. As well, the G/H descriptors of the optimized complexes, MCP drug, and $Al_{12}P_{12}$ nanocage are introduced as $M_{\mathrm{MCP}\bullet\bullet\bullet\mathrm{Al_{12}P_{12}}}$, M_{MCP}, and $M_{\mathrm{Al_{12}P_{12}}}$, respectively. T represents temperature with a value of 310.15 K. Based on frequency calculations, IR and Raman spectra were generated for all optimized complexes. The desorption process was examined for all considered complexes in terms of recovery time that could be assessed according to equation (20).

$$t = \nu^{-1}\, exp(-\Delta E_{ads}/KT) \tag{20}$$

where the attempt frequency of 10^{-18} s^{-1} is represented by ν^{-1} [47], and K refers to the Boltzmann's constant.

Additional comparative elucidation between the adsorption proficiency of the $Al_{12}P_{12}$ and $Al_{12}N_{12}$ nanocages toward MCP drug was herein established. Geometrical optimization was performed for the MCP···$Al_{12}N_{12}$ complex within different configurations. Adsorption energy was then calculated for the optimized structures of the MCP···$Al_{12}N_{12}$ complex. All DFT calculations were employed with the aid of the Gaussian 09 package [48]. All visualizations were accomplished using the Visual Molecular Dynamics (VMD) program [49].

3. Results and discussion

3.1. ESP analysis

Upon geometry optimization calculations, the obtained structures were subjected to ESP analysis. The optimized monomers are displayed in Fig. 1, as previously recommended in the literature [50]. ESP surface was investigated by generating maps of MEP and extracting the maximum and minimum electrostatic potential ($V_{s,max}$ and $V_{s,min}$, respectively) values. Regarding ESP analysis, the

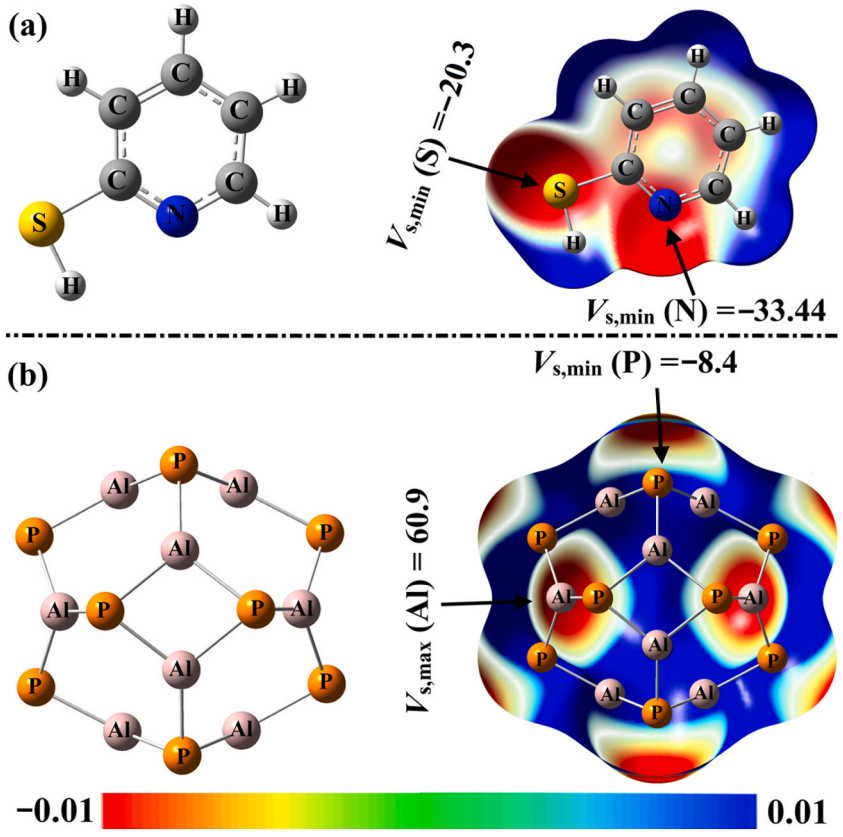

Fig. 1. Optimized geometries and MEP maps of the (a) MCP drug and (b) $Al_{12}P_{12}$ nanocage. $V_{s,min}/V_{s,max}$ values are given by kcal/mol.

electrophilic sites are characterized by blue color along with positive electrostatic potential extrema, while red color and negative electrostatic potential extrema are ascribed to the nucleophilic sites. Fig. 1(a and b) displays MEP maps and $V_{s,min}/V_{s,max}$ values for the optimized structures of the MCP and $Al_{12}P_{12}$.

In the optimized structure of the nanocage, the Al–P bond length was found to be 2.27 and 2.32 Å between hexagonal-hexagonal and hexagonal-tetragonal rings, respectively. The obtained Al–P bond lengths were endorsed by a previous study [25]. Further, the optimized $Al_{12}P_{12}$ nanocage showed 98.92° and 130.27° bond angles for P–Al–P in tetragonal and hexagonal rings, respectively.

The visualized MEP maps plotted in Fig. 1(a and b) showed nucleophilic (i.e., negative) and electrophilic (i.e., positive) regions around the molecular surfaces of MCP/$Al_{12}P_{12}$ systems using red and blue colors, respectively. For the MCP drug, two negative red-colored sites were detected above N and S atoms with $V_{s,min}$ values of −33.4 and −20.3 kcal/mol, respectively. Further, in the case of $Al_{12}P_{12}$ nanocage, positive blue-colored regions were observed around Al atoms, while negative ones were over the P atom. As numerical evidence, the $V_{s,max}$ for Al and $V_{s,min}$ for P were found to be 60.9 and −8.4 kcal/mol in the $Al_{12}P_{12}$ nanocage, respectively.

3.2. Adsorption process

To pursue the targeted adsorption process, the MCP drug-loading step over the surface of the $Al_{12}P_{12}$ nanocage was executed. Geometry optimization was performed for the MCP···$Al_{12}P_{12}$ complex at all possible adsorption sites (Figure S1), giving three preferable configurations, namely, A, B, and C (Fig. 2(a–c)). Upon frequency calculations, no imaginary frequencies were found for those three configurations, confirming that the selected structures were true minima. Adsorption energy (E_{ads}) values were then assessed for the optimized complexes, as illustrated in equation (1). Table 1 summarizes the obtained energetic values along with the MCP···Al equilibrium distances.

According to the enrolled data in Table 1, the preferable adsorption process of the MCP drug over the $Al_{12}P_{12}$ nanocage was verified by short equilibrium distances (d) and negative adsorption energy (E_{ads}) values. Thus, it was endorsed that the MCP drug was favorably adsorbed on the exterior surface of the $Al_{12}P_{12}$ nanocage, which agrees with previous studies [51,52]. Evidently, the negative adsorption energy (E_{ads}) values of the MCP···$Al_{12}P_{12}$ complex within the investigated configurations decreased as follows A > B > C. Comparatively, the MCP···$Al_{12}P_{12}$ complex within configuration A was found with a shorter equilibrium distance than other investigated configurations (see Fig. 2 and Table 1) and accordingly showed the highest negative E_{ads} with a value of −27.71 kcal/mol. Conspicuously, adsorption energy values showed a reverse correlation with equilibrium distances. Numerically, the MCP···Al equilibrium distances within the configurations A, B, and C of the MCP···$Al_{12}P_{12}$ complex were 2.05, 2.07, and 2.55 Å, along with E_{ads} values of −27.71, −26.41, and −13.90 kcal/mol, respectively.

3.3. SAPT calculations

SAPT analysis has been considered a dependable energy decomposition analysis method that dissects the total energy into its main physical components. For the studied MCP···$Al_{12}P_{12}$ complexes, SAPT energies were evaluated using equations (2)–(6), and the obtained energetic components were extracted (Fig. 3).

As shown in Fig. 3(a–c), electrostatic energy (E_{elst}) had the highest attractive contributions to the adsorption process with values up to −74.36 kcal/mol. Further, the dispersion (E_{dis}) and induction (E_{ind}) components were also noticed with preferable negative values. In contrast, an unfavorable contribution was exhibited by exchange forces (E_{exch}). For example, the E_{elst}, E_{exch}, E_{dis}, and E_{ind} values were −73.70, 89.60, −26.92, and −22.34 kcal/mol for the MCP···$Al_{12}P_{12}$ complex within configuration A.

3.4. QTAIM and NCI calculations

QTAIM is a comprehensive topology interpretation tool to reveal the character of the intermolecular interactions within

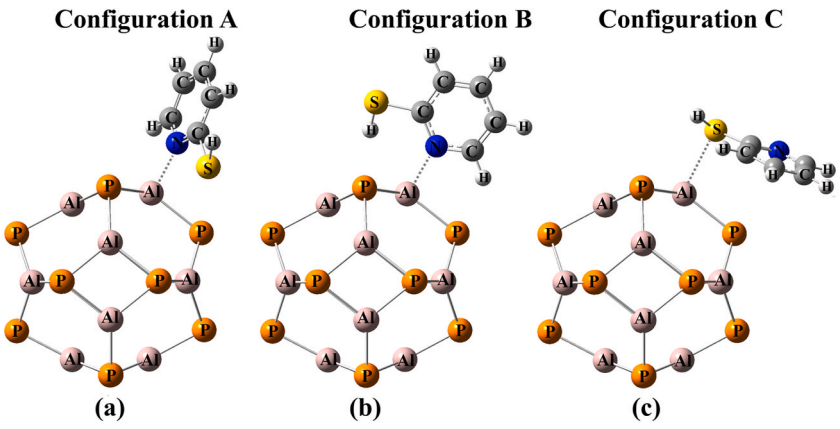

Fig. 2. Optimized structures of the MCP···$Al_{12}P_{12}$ complex within (a) configuration A, (b) configuration B, and (c) configuration C.

Table 1
Calculated values of adsorption (E_{ads}) energy of the optimized MCP···$Al_{12}P_{12}$ complex within configurations A, B, and C. The equilibrium distances (d) are in Å, and the energetic values (E_{ads}) are in kcal/mol.

Complex	Configuration	d	E_{ads}
MCP···$Al_{12}P_{12}$	**A**	2.05	−27.71
	B	2.07	−26.41
	C	2.55	−13.90

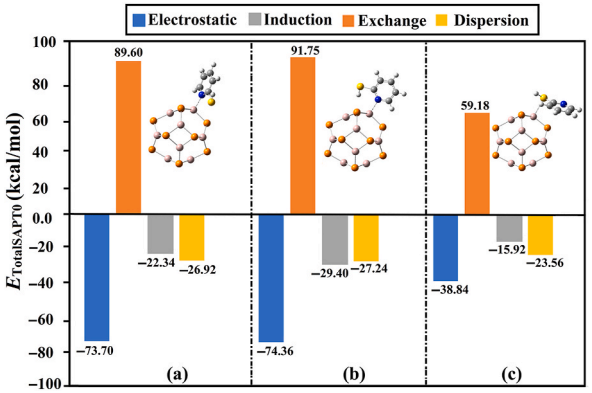

Fig. 3. Graphical illustration of total SAPT0 energy components, including electrostatic (E_{elst}), dispersion (E_{disp}), induction (E_{ind}), and exchange (E_{exch}), of the MCP···$Al_{12}P_{12}$ optimized complex within (a) configuration A, (b) configuration B, and (c) configuration C. The computed energetic quantities are in kcal/mol.

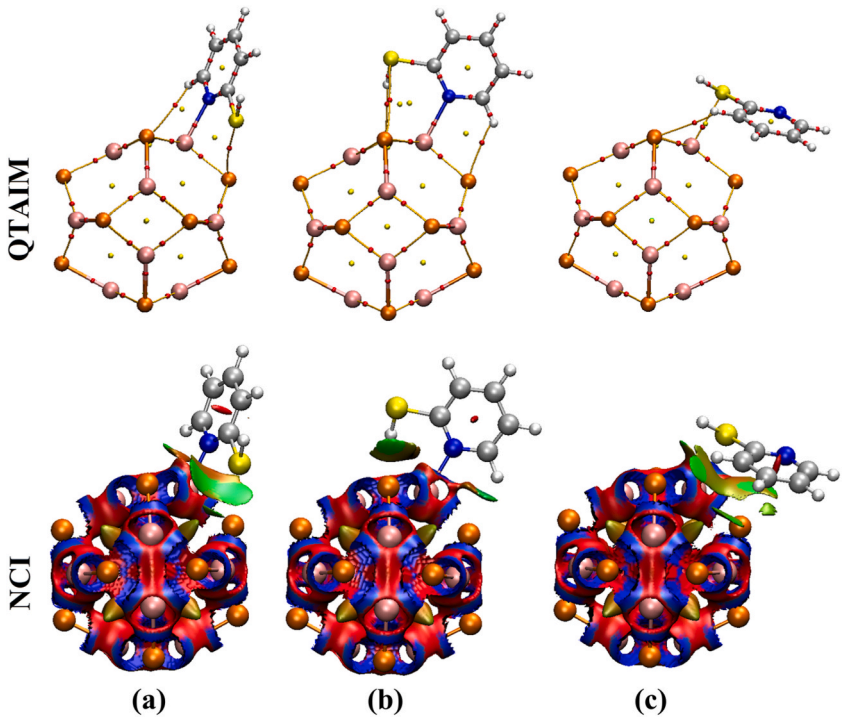

Fig. 4. QTAIM and 3D NCI diagrams of the MCP···$Al_{12}P_{12}$ complex within (a) configuration A, (b) configuration B, and (c) configuration C. Bond paths are presented by lines, while bond and ring critical points are characterized by red and yellow circles. 3D NCI isosurfaces are plotted using a 0.50 au value of reduced density gradient and colored from blue (−0.035 au) to red (0.020 au) according to the sign (λ_2)ρ values. (For interpretation of the references to color in this figure legend, the reader is referred to the Web version of this article.)

MCP···$Al_{12}P_{12}$ complexes [53]. Considering QTAIM, bond paths (BPs) and bond critical points (BCPs) were generated, and topological features were calculated (Fig. 4 and Table 2). Considering the topological features, Laplacian ($\nabla^2\rho_b$), electron density (ρ_b), local potential electron energy density (V_b), total energy density (H_b), kinetic electron density (G_b), and negative ratio of potential, and kinetic electron energy density ($-G_b/V_b$) were computed and are gathered in Table 2. Along with QATIM, noncovalent interactions (NCI) index analysis provides a method to illustrate the origin of interactions between chemical species. 3D NCI isosurfaces and 2D reduced density gradient (RDG) graphs were plotted for the inspected complexes (Fig. 4 and S2, respectively).

From Fig. 4(a–c), QTAIM diagrams revealed the occurrence of the adsorption of the MCP drug over the $Al_{12}P_{12}$ nanocage via the displayed bond paths (BPs) and bond critical points (BCPs). According to the H_b, $\nabla^2\rho_b$, ρ_b, and $-G_b/V_b$ values listed in Table 2, the partial covalent and electrostatic natures were confirmed for the MCP···$Al_{12}P_{12}$ complex within all the investigated configurations. Furthermore, the obtained values of $\nabla^2\rho_b$ and ρ_b were directly correlated with the adsorption energy (see Table 1), which agrees with a previous study [54]. For instance, $\nabla^2\rho_b$ values of the MCP···$Al_{12}P_{12}$ complex within configurations A, B, and C were 0.2689, 0.2425, and 0.0730 au, and the analogical E_{ads} values were −27.71, −26.41, and −13.90 kcal/mol, respectively. As per the above discussion, the studied MCP···$Al_{12}P_{12}$ interactions could be classified as partial covalent and electrostatic.

According to 3D NCI isosurfaces, the potentiality of $Al_{12}P_{12}$ nanocage toward adsorbing MCP drug was obviously illustrated via the colored isosurfaces between the drug and nanocage (Fig. 4(a–c)). It was important to underline that the alteration in color and size of the 3D NCI isosurfaces was consistent with the energetic pattern. As shown in Figure S2, 2D NCI spikes were denoted at sign $(\lambda_2)\rho$ values lower than 0.01 au, indicating the occurrence of attractive interactions within the studied complexes, which is in line with a previous study [55].

3.5. Electronic parameters

To sufficiently demonstrate the electronic parameters of the MCP drug and $Al_{12}P_{12}$ nanocage, frontier molecular orbitals (FMOs) theory was applied. According to FMOs, the energies of the molecular orbitals, including the highest occupied molecular orbitals (E_{HOMO}) and the lowest unoccupied molecular orbitals (E_{LUMO}), were computed before and after the adsorption process. The Fermi level (E_{FL}) and energy gap (E_{gap}) were further calculated according to equations (7) and (8), respectively. In the essence of FMOs method, visual representations of HOMO and LUMO energy levels before and after the adsorption of MCP drug were generated and are visualized in Figs. 5 and 6, respectively. Further, the calculated values of E_{HOMO}, E_{LUMO}, E_{FL}, and E_{gap} are gathered in Table 3.

Notably, HOMO and LUMO orbitals were distributed over electronegative and electropositive regions, respectively. As shown in Fig. 5(a), HOMO orbitals were located above N and S atoms of the MCP drug, while LUMO levels were observed around the H and C atoms. Turning to the $Al_{12}P_{12}$ nanocage, the HOMO and LUMO orbitals were generally accumulated around P and Al atoms, respectively (Fig. 5(b)).

Following the adsorption process of the MCP drug over the $Al_{12}P_{12}$ nanocage, the distribution patterns of HOMO and LUMO were noticeably altered (see Fig. 6(a–c)), reflecting the adsorbing ability of $Al_{12}P_{12}$ nanocage toward the MCP drug. Interestingly, the HOMO and LUMO orbitals were localized around the $Al_{12}P_{12}$ nanocage in all studied complexes. Further, the redistribution of HOMO and LUMO levels after the adsorption process of the MCP drug illustrated the occurrence of charge transfer within the studied complexes, which is in line with the earlier reported results in the literature [56].

By analyzing data in Table 3, changes in E_{HOMO}, E_{LUMO}, E_{FL}, and E_{gap} values after the adsorption of the MCP drug were noted, demonstrating the occurrence of the adsorption process. For instance, E_{HOMO} values were found to be −7.77 and −7.24/–7.29/–7.48 eV for the isolated $Al_{12}P_{12}$ nanocage and its corresponding complex with MCP drug within configurations A/B/C, respectively. As well, the E_{gap} values diminished upon the adsorption process, which in turn increased the conductivity (see equation (16) in the Computational Methods). Illustratively, E_{gap} of $Al_{12}P_{12}$ nanocage was found to be 4.72 eV and decreased to 4.70, 4.66, and 4.61 eV for MCP···$Al_{12}P_{12}$ complex within configurations A, B, and C, respectively. Such conductivity increase confirmed that the $Al_{12}P_{12}$ nanocage is a promising electrochemical biosensor for MCP drug. Obviously, the E_{FL} value of $Al_{12}P_{12}$ nanocage was changed upon the MCP drug-loading process from −5.41 eV to −4.89/–4.96/–5.18 eV for configurations A/B/C.

3.6. Global indices of reactivity

To deeply investigate the effect of the adsorption process on the reactivity indices of the MCP drug and $Al_{12}P_{12}$ nanocage, the ionization potential (*IP*), electron affinity (*EA*), global hardness (η), chemical potential (μ), global softness (*S*), electrophilicity index (ω), and work function (Φ) were calculated using equations (9)–(15), respectively. The obtained descriptors for isolated systems and their corresponding complexes are collected in Table 4.

Table 2
QTAIM topological features of the MCP···$Al_{12}P_{12}$ optimized complex within configurations A, B, and C, including Laplacian ($\nabla^2\rho_b$), electron density (ρ_b), local potential electron energy density (V_b), total energy density (H_b), kinetic electron density (G_b), and the negative ratio of kinetic and potential electron energy density ($-G_b/V_b$). All parameters are in au.

Complex	Configuration	$\nabla^2\rho_b$	ρ_b	V_b	H_b	G_b	$-G_b/V_b$
MCP···$Al_{12}P_{12}$	**A**	0.2689	0.0529	−0.0729	−0.0028	0.0701	0.9613
	B	0.2425	0.0505	−0.0671	−0.0032	0.0639	0.9518
	C	0.0730	0.0344	−0.0345	−0.0081	0.0264	0.7646

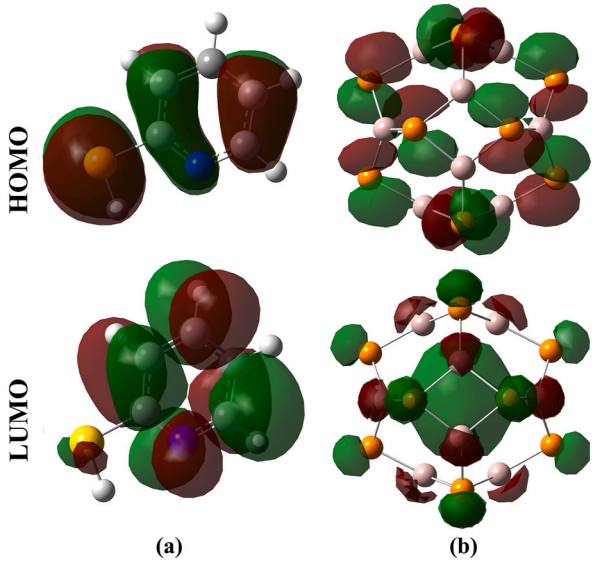

Fig. 5. The distribution of HOMO and LUMO of (a) MCP and (b) $Al_{12}P_{12}$ molecular surfaces.

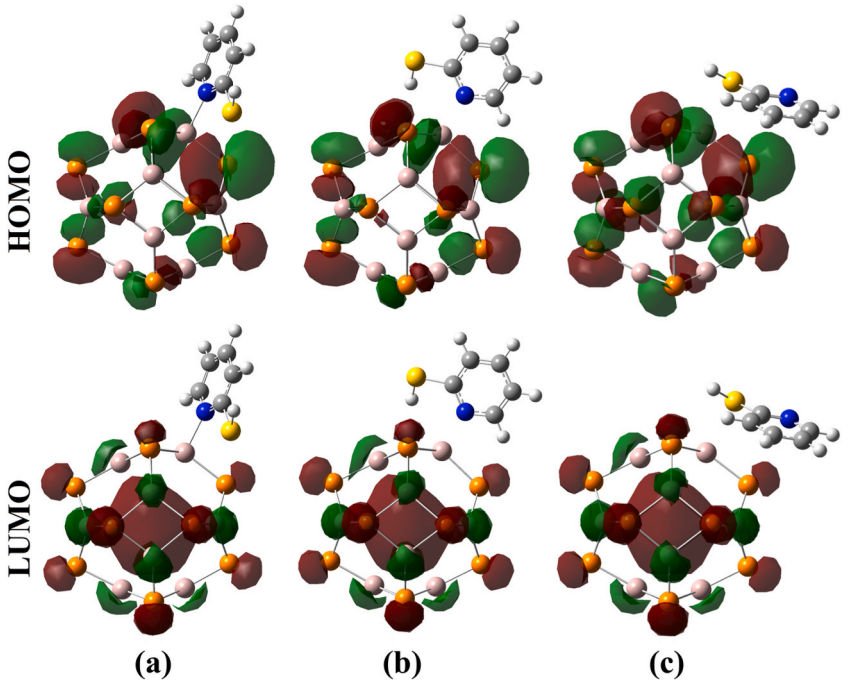

Fig. 6. The distribution of molecular orbitals (HOMO and LUMO) of the MCP···$Al_{12}P_{12}$ optimized complex within (a) configuration A, (b) configuration B, and (c) configuration C.

Table 3
Calculated E_{HOMO}, E_{LUMO}, E_{FL}, and E_{gap} values of the MCP and $Al_{12}P_{12}$ before and after the adsorption process. The computed energies are given in eV.

System	Configuration	E_{HOMO} (eV)	E_{LUMO} (eV)	E_{FL} (eV)	E_{gap} (eV)
MCP		−7.74	−0.22	−3.98	7.52
$Al_{12}P_{12}$		−7.77	−3.05	−5.41	4.72
MCP···$Al_{12}P_{12}$	**A**	−7.24	−2.54	−4.89	4.70
	B	−7.29	−2.63	−4.96	4.66
	C	−7.48	−2.87	−5.18	4.61

Table 4
Global indices of reactivity for the MCP and $Al_{12}P_{12}$ molecules and their corresponding complexes.

System	Configuration	*IP* (eV)	*EA* (eV)	μ (eV)	η (eV)	S (eV^{-1})	ω (eV)	Φ (eV)
MCP		7.74	0.22	−3.98	3.76	0.27	2.10	3.98
$Al_{12}P_{12}$		7.77	3.05	−5.41	2.36	0.42	6.20	5.41
MCP···$Al_{12}P_{12}$	**A**	7.24	2.54	−4.89	2.35	0.43	5.08	4.89
	B	7.29	2.63	−4.96	2.33	0.43	5.28	4.96
	C	7.48	2.87	−5.18	2.31	0.43	5.81	5.18

From data presented in Table 4, noticeable changes in global indices of reactivity values were found for the isolated MCP/$Al_{12}P_{12}$ systems and their corresponding complexes. As numerical evidence, *IP* values were 7.77 and 7.24/7.29/7.48 eV for the $Al_{12}P_{12}$ nanocage before and after the adsorption process within A/B/C configurations, respectively. It was intriguing to note that the decrement in *IP* values was consistent with E_{HOMO} values (see Table 3).

Notably, a decrement in η values was observed upon the adsorption of the MCP drug over the $Al_{12}P_{12}$ nanocage, indicating the occurrence of the adsorption process. For example, η values were 2.36 and 2.35/2.33/2.31 eV for $Al_{12}P_{12}$ nanocage and MCP···$Al_{12}P_{12}$ complex within A/B/C configurations, respectively.

3.7. DOS analysis

The density of state (DOS) analysis was executed to demonstrate the effect of the MCP adsorption process on the electronic properties of the $Al_{12}P_{12}$ nanocage by generating total and partial DOS (TDOS and PDOS, respectively). TDOS and PDOS diagrams were

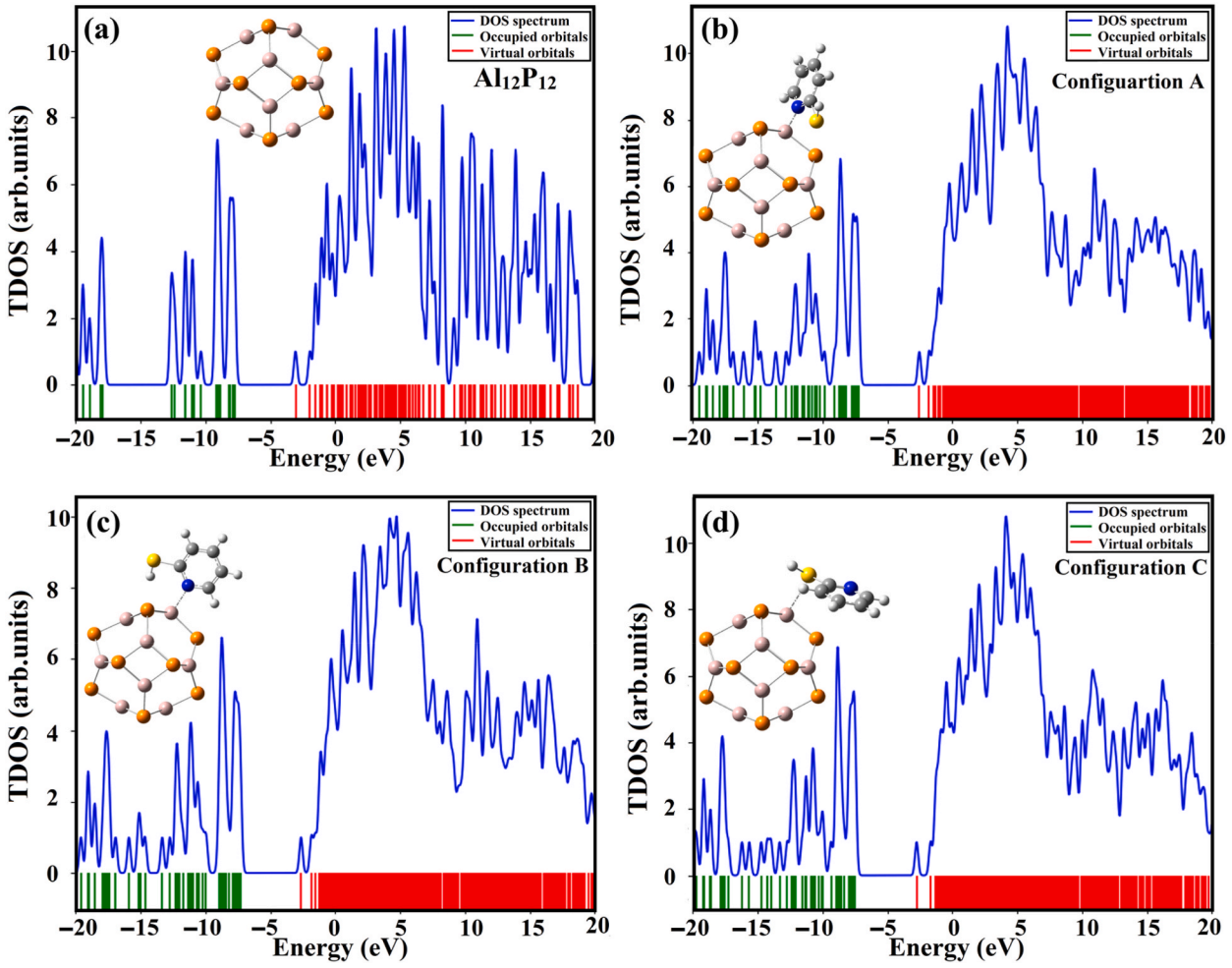

Fig. 7. TDOS diagrams of (a) isolated $Al_{12}P_{12}$ nanocage, along with MCP···$Al_{12}P_{12}$ complex within (b) configuration A, (c) configuration B, and (d) configuration C.

extracted for the isolated nanocage and its corresponding complexes (Fig. 7 and S3, respectively).

As evident in Fig. 7(a–d), TDOS diagrams declared observable changes in the electronic characteristics of the $Al_{12}P_{12}$ nanocage after the adsorption of the MCP drug. It was noticed that the displacement of HOMO and LUMO peaks could be a consequence of the MCP adsorption. Figure S3 addressed the existence of a significant overlap between the PDOS of $N_s/N_p/S_s/S_p$ and Al_s/Al_p orbitals relevant to the drug and nanocage, respectively. These findings highlighted the contributions of the *s*- and *p*-orbitals to the occurrence of the adsorption process.

3.8. Solvent effect

To unveil the effect of water solvent on the MCP drug adsorption process, the geometries of isolated MCP, $Al_{12}P_{12}$, and their corresponding complexes were optimized in a water medium. The favorability of the adsorption process within the MCP···$Al_{12}P_{12}$ optimized complexes in water was then estimated by means of adsorption ($E_{ads}^{solvent}$) and solvation (ΔE_{solv}) energy values (see equation (17) in the Computational Methods). Table 5 provides the computed values of $E_{ads}^{solvent}$ and ΔE_{solv} for the MCP···$Al_{12}P_{12}$ complex within configurations A, B, and C.

As listed in Table 5, $E_{ads}^{solvent}$ and ΔE_{solv} energies exhibited negative values, demonstrating that the studied adsorption process occurs favorably in the water medium. More preferential $E_{ads}^{solvent}$ with a value of −29.17 kcal/mol was ascribed to the MCP···$Al_{12}P_{12}$ complex within configuration A, which was consistent with the E_{ads} pattern in the gas phase (Table 1). Inspecting substantial negative ΔE_{solv} values, further preferability of the adsorption process in the water medium was denoted more plainly compared with the gas phase.

3.9. Thermodynamic parameters

To ascertain the thermodynamic favorability of the MCP drug adsorption process, thermodynamic parameters, including Gibbs free energy (ΔG), enthalpy change (ΔH), and entropy change (ΔS), were computed according to equations (18) and (19) and are summarized in Table 6.

Table 6 provides insight into the spontaneous nature of the considered adsorption process within the investigated complexes according to negative values of ΔG. As well, the exothermic nature was also confirmed through negative values of ΔH that ranged from −12.64 to −26.00 kcal/mol. Plainly, substantial negative ΔG and ΔH values were noticed for configuration A compared with other modeled configurations, which fits a similar pattern to that of the adsorption energy values (see Table 1). For instance, ΔG and ΔH values were found to be −13.41 and −26.00 kcal/mol for MCP···$Al_{12}P_{12}$ complex within configuration A, respectively. In comparison, small negative values for ΔS were denoted for the MCP···$Al_{12}P_{12}$ complex within all the considered configurations. In conclusion, the thermodynamic parameters demonstrated the exothermicity and spontaneity of the adsorption process of the MCP drug on the $Al_{12}P_{12}$ nanocage.

3.10. IR and Raman spectra

Infrared (IR) and Raman spectra are informative techniques for detecting changes in chemical structures by identifying their functional groups. IR and Raman spectra of the $Al_{12}P_{12}$ nanocage and the MCP···$Al_{12}P_{12}$ complex within configurations A, B, and C were generated and are depicted in Fig. 8.

As shown in Fig. 8(a–d), the IR spectra were noticed with an obvious change in the stretching bends of the $Al_{12}P_{12}$ nanocage after the adsorption of the MCP drug. For the MCP···$Al_{12}P_{12}$ complex within configurations A, B, and C, new peaks were observed, affirming the effectiveness of the MCP adsorption over the $Al_{12}P_{12}$ nanocage. Turning to Raman spectra, significant differences were detected for $Al_{12}P_{12}$ nanocage after contact with the MCP drug. The emerging changes in the IR and Raman spectra ensured the promising application of $Al_{12}P_{12}$ nanocage in the adsorption process of MCP drug within the investigated configurations.

3.11. Recovery time

The recovery time (τ) is paramount for assessing the difficulty of releasing the drug from the nanocage surface. Herein, τ of the MCP···$Al_{12}P_{12}$ complex within configurations A, B, and C were computed (see equation (20) in the Computational Methods) and showed values of 3.22×10^{7}, 3.91×10^{6}, and 6.10×10^{-3} μs, respectively. Notably, the longest recovery time was obtained for configuration A, which exhibited the most favorable adsorption energy ($E_{ads} = -27.71$ kcal/mol). While configuration C had a short recovery time, ensuring the feasibility of separating the drug from the nanocage surface. The obtained correlation between the longer

Table 5
Adsorption ($E_{ads}^{solvent}$) and solvation (ΔE_{solv}) energies for the MCP···$Al_{12}P_{12}$ complex within configurations A, B, and C in the water medium. All values are in kcal/mol.

Complex	Configuration	$E_{ads}^{solvent}$ (kcal/mol)	ΔE_{solv} (kcal/mol)
MCP···$Al_{12}P_{12}$	**A**	−29.17	−17.75
	B	−25.69	−15.57
	C	−13.94	−16.12

Table 6
Gibbs free energy (Δ*G*), enthalpy change (Δ*H*), and entropy change (Δ*S*) of MCP···$Al_{12}P_{12}$ complex within configurations A, B, and C. All parameters are in kcal/mol.

Complex	Configuration	Δ*G*	Δ*H*	Δ*S*
MCP···$Al_{12}P_{12}$	**A**	−13.41	−26.00	−0.042
	B	−12.35	−24.90	−0.042
	C	−0.89	−12.64	−0.039

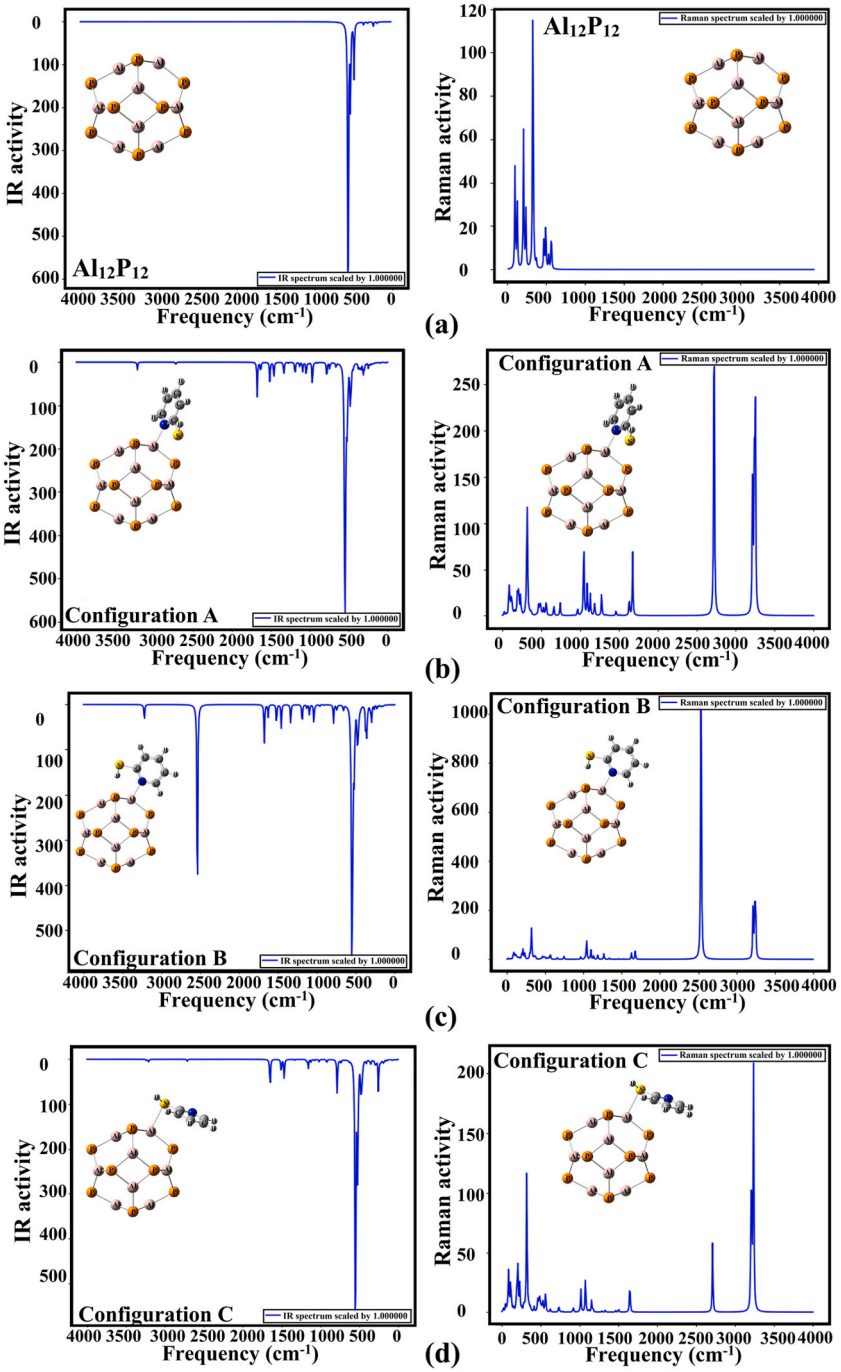

Fig. 8. Infrared radiation (IR) and Raman spectra of (a) isolated $Al_{12}P_{12}$ nanocage along with MCP···$Al_{12}P_{12}$ complex within (b) configuration A, (c) configuration B, and (d) configuration C.

recovery time and the higher negative adsorption energy values coincided with the literature [57,58].

3.12. $Al_{12}N_{12}$ vs $Al_{12}P_{12}$ nanocages

To provide a comparative insight into the potentiality of the $Al_{12}P_{12}$ nanocage with its relative aluminium-based nanocage, the $Al_{12}N_{12}$ nanocage was adopted as a candidate for adsorbing MCP drug. For the $Al_{12}N_{12}$ nanocage, an MEP map was generated (Fig. 9 (a)).

As shown in Fig. 9(a), the $Al_{12}N_{12}$ nanocage showed a strong electrophilic character compared to $Al_{12}P_{12}$ nanocage. Numerically, the blue (positive) regions above Al atoms were found with $V_{s,max}$ value of 101.2 kcal/mol, while red regions around N atoms showed $V_{s,min}$ with a value of −35.5 kcal/mol. Obviously, the negativity of N atoms of $Al_{12}N_{12}$ is higher than P atoms of the $Al_{12}P_{12}$ analog. Quantitatively, the $V_{s,min}$ values of N and P atoms were −35.5 and −8.4 kcal/mol.

As a point of comparison, the MCP···$Al_{12}N_{12}$ complex was optimized within all plausible configurations at the same level of theory utilized for the MCP···$Al_{12}P_{12}$ counterpart (Figure S4). The preferable structures are displayed in Fig. 9(b). Based on the optimized complexes, the adsorption energies were calculated.

According to the results, the MCP···$Al_{12}N_{12}$ complexes were denoted with negative adsorption energies values up to −76.42 kcal/mol. From a comparative point of view, the E_{ads} values for the MCP···$Al_{12}N_{12}$ complex within the modeled configurations were found to be more negative than their counterparts of the MCP···$Al_{12}P_{12}$ complex. Unlike the MCP···$Al_{12}P_{12}$ complex, the MCP···$Al_{12}N_{12}$ complex within configuration B exhibited the most negative E_{ads} value of −76.42 kcal/mol. Inspecting the optimized structure of configuration B revealed that the MCP drug was distorted by hydrogen transfer to the $Al_{12}N_{12}$ nanocage (Fig. 9(b)). Thus, the desorption process would not be feasible, leading to an incomplete MCP adsorption on the $Al_{12}N_{12}$ nanocage. These results revealed the lower proficiency of the $Al_{12}N_{12}$ nanocage toward adsorbing MCP drug compared with the $Al_{12}P_{12}$ analog.

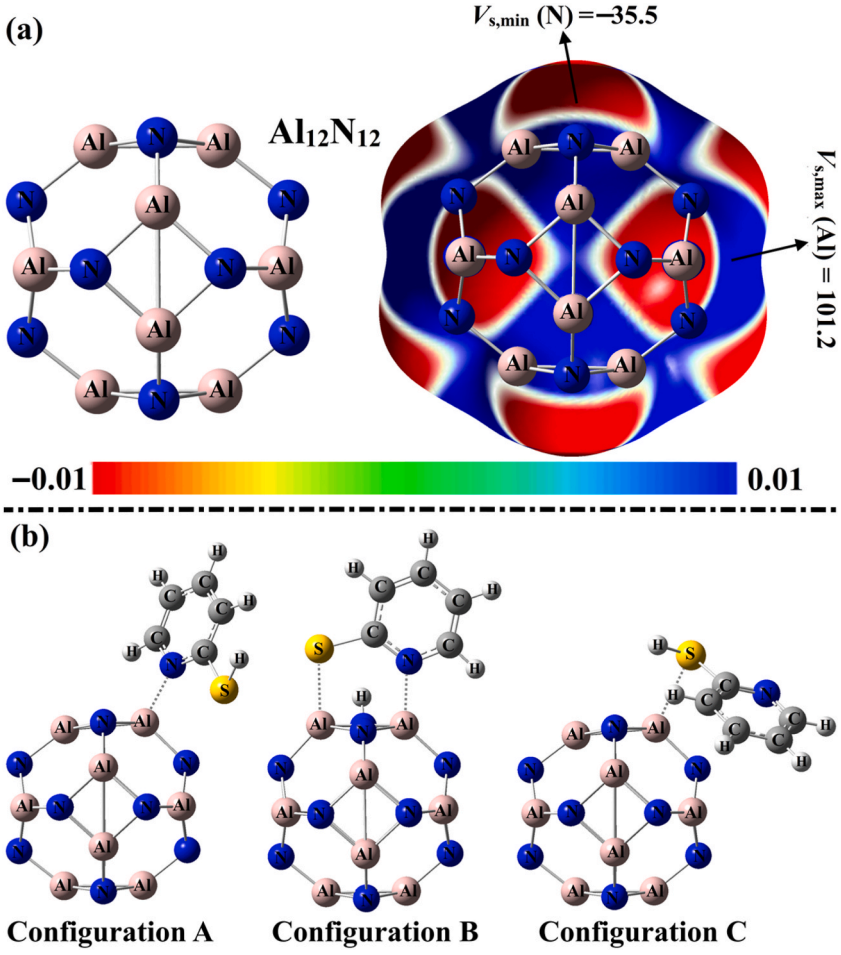

Fig. 9. (a) Optimized structure of $Al_{12}N_{12}$ supplemented by the graphed MEP map, and (b) optimized structures of the MCP···$Al_{12}N_{12}$ complex within configurations A, B, and C.

4. Conclusion

The versatility of the $Al_{12}P_{12}$ nanocage to engage in the adsorption of the 2-Mercaptopyridine (MCP) drug was examined within configurations A, B, and C by utilizing DFT calculations. The ESP analysis revealed the existence of notable nucleophilic sites over the N and S atoms of the MCP drug. In comparison, eminent electrophilic sites were observed over the Al atoms in the $Al_{12}P_{12}$ nanocage. The obtained findings highlighted the most negative adsorption energy in the case of the MCP···$Al_{12}P_{12}$ complex within configuration A, with a value of −27.71 kcal/mol. Upon SAPT results, the electrostatic forces were announced to be the dominant force beyond the adsorption process. In the framework of FMO analysis, superb changes in the distribution of HOMO and LUMO patterns were observed for the $Al_{12}P_{12}$ nanocage compared to its complexes with the MCP drug. Alteration in E_{HOMO} and E_{LUMO} upon the adsorption process reflected the origin of major changes in electronic features such as energy gap (E_{gap}) and Fermi level (E_{FL}). As well, the spontaneous and exothermic natures were accentuated by calculating the thermodynamic parameters. Significant negative solvation energy values were observed, confirming the further preferentiality of the adsorption process in water solvent more than in the gas phase. Short recovery time values ensured the ability of the $Al_{12}P_{12}$ nanocage to desorb the loaded MCP drug within the MCP···$Al_{12}P_{12}$ complex. The noticeable potentiality of the $Al_{12}P_{12}$ nanocage toward adsorbing MCP drug was recognized with higher proficiency compared with the $Al_{12}N_{12}$ analog. In comparison to the $Al_{12}P_{12}$ nanocage, the lower applicability of the $Al_{12}N_{12}$ nanocage toward drug adsorption was addressed owing to the occurrence of structural distortion.

Author contribution statement

Lamiaa A. Mohamed, Peter A. Sidhom, Shaban R. M. Sayed, Mohamed K. Abd El-Rahman, Eslam Dabbish, Tamer Shoeib, and Mahmoud A. A. Ibrahim: Conceived and designed the experiments; Contributed reagents, materials, analysis tools or data; Reviewed the paper. Al-shimaa S. M. Rady: Performed the experiments; Analyzed and interpreted the data; Wrote the paper. Nayra A. M. Moussa: Analyzed and interpreted the data; Reviewed the paper.

Data availability statement

Data included in article/supplementary material/referenced in article.

Additional information

Supplementary content related to this article has been published online at [URL].

Declaration of competing interest

The authors declare that they have no known competing financial interests or personal relationships that could have appeared to influence the work reported in this paper.

Acknowledgements

The authors extend their appreciation to the Researchers Supporting Project number (RSPD2023R743), King Saud University, Riyadh, Saudi Arabia, for funding this work. The computational work was conducted on CompChem GPU/CPU hybrid cluster (hpc.compchem.net) supported by the Science and Technology Development Fund, STDF, Egypt, Grants No. 5480 & 7972.

Appendix A. Supplementary data

Supplementary data related to this article can be found at https://doi.org/10.1016/j.heliyon.2023.e18690.

References

[1] N. Chakraborty, D. Jha, I. Roy, P. Kumar, S.S. Gaurav, K. Marimuthu, O.T. Ng, R. Lakshminarayanan, N.K. Verma, H.K. Gautam, Nanobiotics against antimicrobial resistance: harnessing the power of nanoscale materials and technologies, J. Nanobiotechnology 20 (2022) 375, https://doi.org/10.1186/s12951-022-01573-9.

[2] A. Yadav, K. Mondal, A. Gupta, Biomedical application of ZnO nanoscale materials, in: K. Mondal (Ed.), Metal Oxides for Biomedical and Biosensor Applications, Elsevier, 2022, pp. 407–435.

[3] N. Khaki, S. Fosshat, P. Pourhakkak, R.D. Thanoon, A.T. Jalil, L. Wu, Sensing of acetaminophen drug using Zn-doped boron nitride nanocones: a DFT inspection, Biotechnol. Appl. Biochem. 194 (2022) 2481–2491, https://doi.org/10.1007/s12010-022-03830-x.

[4] M.M. Kadhim, N. Sheibanian, D. Ashoori, M. Sadri, B. Tavakoli-Far, R. Khadivi, R. Akhavan-Sigari, The drug delivery of hydrea anticancer by a nanocone-oxide: computational assessments, Comput. Theor. Chem. 1215 (2022), 113843, https://doi.org/10.1016/j.comptc.2022.113843.

[5] Y.A. Atia, D.O. Bokov, K.R. Zinnatullovich, M.M. Kadhim, W. Suksatan, W.K. Abdelbasset, H.A. Hammoodi, Y.F. Mustafa, Y. Cao, The role of amino acid functionalization for improvement of adsorption Thioguanine anticancer drugs on the boron nitride nanotubes for drug delivery, Mater. Chem. Phys. 278 (2022), 125664, https://doi.org/10.1016/j.matchemphys.2021.125664.

[6] F. Abolhasani Zadeh, S. Abdalkareem Jasim, M. Javed Ansari, D. Olegovich Bokov, G. Yasin, L. Thangavelu, M. Derakhshandeh, Boron carbide nanotube as targeted drug delivery system for melphalan anticancer drug, J. Mol. Liq. 354 (2022), 118796, https://doi.org/10.1016/j.molliq.2022.118796.

[7] E.B. Kalika, K.P. Katin, A.I. Kochaev, S. Kaya, M. Elik, M.M. Maslov, Fluorinated carbon and boron nitride fullerenes for drug Delivery: computational study of structure and adsorption, J. Mol. Liq. 353 (2022), 118773, https://doi.org/10.1016/j.molliq.2022.118773.

[8] O.R. Pop, J.F. Van Staden, Theoretical evaluation of the interactions between metal-phthalocyanines and various fullerenes as delivery systems, Chemistry-Basel 4 (2022) 1016–1027, https://doi.org/10.3390/chemistry4030069.

[9] M. Yousefi, M.S. Rad, R. Shakibazadeh, L. Ghodrati, M.A. Kachoie, Simulating a heteroatomic CBN fullerene-like nanocage towards the drug delivery of fluorouracil, Mol. Simulat. 48 (2022) 1284–1292, https://doi.org/10.1080/08927022.2022.2086252.

[10] C. Yao, F. Xiang, Z. Xu, Metal oxide nanocage as drug delivery systems for Favipiravir, as an effective drug for the treatment of COVID-19: a computational study, J. Mol. Model. 28 (2022) 64, https://doi.org/10.1007/s00894-022-05054-6.

[11] M.A.A. Ibrahim, A.-s.S.M. Rady, N.A.M. Moussa, M.N. Ahmed, P.A. Sidhom, A.M. Shawky, A.M. Alqahtani, L.A. Mohamed, Investigation of aluminum nitride nanocarrier for drug delivery process of Favipiravir: a DFT study, J. Mol. Liq. 372 (2023), 121209, https://doi.org/10.1016/j.molliq.2023.121209.

[12] M.A.A. Ibrahim, A.S.M. Rady, A.M.A. Mandarawe, L.A. Mohamed, A.M. Shawky, T.H.A. Hasanin, P.A. Sidhom, M.E.S. Soliman, N.A.M. Moussa, Adsorption of chlormethine anti-cancer drug on pure and aluminum-doped boron nitride nanocarriers: a comparative DFT study, Pharmaceuticals 15 (2022) 1181, https://doi.org/10.3390/ph15101181.

[13] M.A.A. Ibrahim, A.S.M. Rady, L.A. Mohamed, A.M. Shawky, T.H.A. Hasanin, P.A. Sidhom, N.A.M. Moussa, Adsorption of Molnupiravir anti-COVID-19 drug over B(12)N(12) and Al(12)N(12) nanocarriers: a DFT study, J. Biomol. Struct. Dyn. (2023) 1–15, https://doi.org/10.1080/07391102.2023.2169763.

[14] B. Tousian, M.H. Ghasemi, A.R. Khosravi, Targeted chitosan nanoparticles embedded into graphene oxide functionalized with caffeic acid as a potential drug delivery system: new insight into cancer therapy, Int. J. Biol. Macromol. 222 (2022) 295–304, https://doi.org/10.1016/j.ijbiomac.2022.09.084.

[15] H. Abu Owida, Biomimetic nanoscale materials for skin cancer therapy and detection, J. Skin Cancer 2022 (2022), 2961996, https://doi.org/10.1155/2022/2961996.

[16] V. Chandrakala, V. Aruna, G. Angajala, Review on metal nanoparticles as nanocarriers: current challenges and perspectives in drug delivery systems, Emergent Mater 5 (2022) 1593–1615, https://doi.org/10.1007/s42247-021-00335-x.

[17] J. Beheshtian, Z. Bagheri, M. Kamfiroozi, A. Ahmadi, A comparative study on the B12N12, Al12N12, B12P12 and Al12P12 fullerene-like cages, J. Mol. Model. 18 (2012) 2653–2658, https://doi.org/10.1007/s00894-011-1286-y.

[18] P.Y. Feng, K. Balasubramanian, Spectroscopic properties of Al2P2, Al2P2+, and Al2P2- and comparison with their Ga and in analogues, J. Phys. Chem. A 103 (1999) 9093–9099, https://doi.org/10.1021/jp991542+.

[19] E.F. Archibong, R.M. Gregorius, S.A. Alexander, Structures and electron detachment energies of AlP2− and Al2P2, Chem. Phys. Lett. 321 (2000) 253–261, https://doi.org/10.1016/s0009-2614(00)00355-9.

[20] A. Shokuhi Rad, K. Ayub, Adsorption of pyrrole on Al12N12, Al12P12, B12N12, and B12P12 fullerene-like nanocages; a first principles study, Vacuum 131 (2016) 135–141, https://doi.org/10.1016/j.vacuum.2016.06.012.

[21] A. Allangawi, M.A. Gilani, K. Ayub, T. Mahmood, First row transition metal doped B12P12 and Al12P12 nanocages as excellent single atom catalysts for the hydrogen evolution reaction, Int. J. Hydrogen Energy 48 (2023) 16663–16677, https://doi.org/10.1016/j.ijhydene.2023.01.154.

[22] P. Khan, M. Jamshaid, S. Tabassum, S. Perveen, T. Mahmood, K. Ayub, J.C. Yang, M.A. Gilani, Exploring the interaction of ionic liquids with Al12N12 and Al12P12 nanocages for better electrode-electrolyte materials in super capacitors, J. Mol. Liq. 344 (2021), 117828, https://doi.org/10.1016/j.molliq.2021.117828.

[23] F. Khaliq, K. Ayub, T. Mahmood, S. Muhammad, S. Tabassum, M.A. Gilani, First example of lanthanum as dopant on Al12N12 and Al12P12 nanocages for improved electronic and nonlinear optical properties with high stability, Mater. Sci. Semicond. Process. 135 (2021), 106122, https://doi.org/10.1016/j.mssp.2021.106122.

[24] A. Shokuhi Rad, K. Ayub, A comparative density functional theory study of guanine chemisorption on Al12N12, Al12P12, B12N12, and B12P12 nanocages, J. Alloys Compd. 672 (2016) 161–169, https://doi.org/10.1016/j.jallcom.2016.02.139.

[25] R. Padash, M.R. Esfahani, A.S. Rad, The computational quantum mechanical study of sulfamide drug adsorption onto X(12)Y(12) fullerene-like nanocages: detailed DFT and QTAIM investigations, J. Biomol. Struct. Dyn. 39 (2021) 5427–5437, https://doi.org/10.1080/07391102.2020.1792991.

[26] R. Padash, A. Sobhani-Nasab, M. Rahimi-Nasrabadi, M. Mirmotahari, H. Ehrlich, A.S. Rad, M. Peyravi, Is it possible to use X12Y12 (X = Al, B, and Y = N, P) nanocages for drug-delivery systems? A DFT study on the adsorption property of 4-aminopyridine drug, Appl. Phys. A 124 (2018) 1–11, https://doi.org/10.1007/s00339-018-1965-y.

[27] Y. Shyma Mary, Y. Sheena Mary, Z. Ullah, Computational study of sorbic acid drug adsorption onto coronene/fullerene/fullerene-like X12Y12 (X = Al, B and Y = N, P) nanocages: DFT and molecular docking investigations, J. Cluster Sci. 33 (2021) 1809–1819, https://doi.org/10.1007/s10876-021-02106-4.

[28] G. Mehraein, M. Rezaei-Sameti, E. Asgary, M. Aghamohammadi, The effects of Cu, Zn doped, and static electrical field on the interaction of mercaptopyridine drug with B12P12 nanocage: insight from DFT, TD-DFT, J. Mol. Struct. 1248 (2022), 131478, https://doi.org/10.1016/j.molstruc.2021.131478.

[29] M. Rezaei−Sameti, M.J.C.M. Jafari, Effect of Ni and Pd transition metal functionalized on interaction of mercaptopyridine with B12N12 nanocage: NBO, AIM, DFT, TD-DFT study, Chem. Methodol. 4 (2020) 494–513, https://doi.org/10.33945/sami/chemm.2020.4.10.

[30] S. Melandri, L. Evangelisti, A. Maris, W. Caminati, B.M. Giuliano, V. Feyer, K.C. Prince, M. Coreno, Rotational and core level spectroscopies as complementary techniques in tautomeric/conformational studies: the case of 2-mercaptopyridine, J. Am. Chem. Soc. 132 (2010) 10269–10271, https://doi.org/10.1021/ja104484b.

[31] K. Wzgarda-Raj, O. Ksiazkiewicz, M. Palusiak, Co-crystal synthesis of 2-and 4-mercaptopyridines with thiourea and its analogue, trithiocyanuric acid, CrystEngComm 24 (2022) 5340–5347, https://doi.org/10.1039/d2ce00592a.

[32] R.N. Asha, C. Daisy, N. Bhuvanesh, B.R.D. Nayagam, 2,4-bis(bromomethyl)-1,3,5-trimethylbenzene with 2-mercaptopyridine based derivative: synthesis, crystal structure, in vitro anticancer activity, DFT, Hirshfeld surface analysis, antioxidant, DNA binding and molecular docking studies, J. Mol. Struct. 1251 (2022), 131981, https://doi.org/10.1016/j.molstruc.2021.131981.

[33] S.W. Wright, K.N. Hallstrom, A convenient preparation of heteroaryl sulfonamides and sulfonyl fluorides from heteroaryl thiols, J. Org. Chem. 71 (2006) 1080–1084, https://doi.org/10.1021/jo052164+.

[34] J.H. Wedig, C. Mitoma, R.A. Howd, D.W. Thomas, Identification of metabolites from salts of pyridine-2-thiol-1-oxide following intravenous and dermal adminstration to swine, Toxicol. Appl. Pharmacol. 43 (1978) 373–379, https://doi.org/10.1016/0041-008x(78)90016-9.

[35] S.K. Hadjikakou, M.A. Demertzis, M. Kubicki, D. Kovala-Demertzi, Organotin adducts with pyrimidinethione: crystal structure of dimethyldi(pyrimidine-2-thiolato)tin(IV) and diphenyldi(pyrimidine-2-thiolato)tin(IV), Appl. Organomet. Chem. 14 (2000) 727–734, https://doi.org/10.1002/1099-0739, 200011)14:11<727::Aid-Aoc68>3.0.Co;2-H.

[36] M. Hong, H. Geng, M. Niu, F. Wang, D. Li, J. Liu, H. Yin Organotin, IV) complexes derived from Schiff base N'-[(1E)-(2-hydroxy-3-methoxyphenyl)methylidene] pyridine-4-carbohydrazone: synthesis, in vitro cytotoxicities and DNA/BSA interaction, Eur. J. Med. Chem. 86 (2014) 550–561, https://doi.org/10.1016/j.ejmech.2014.08.070.

[37] M. Rezaei-Sameti, S.K. Abdoli, The capability of the pristine and (Sc, Ti) doped Be12O12 nanocluster to detect and adsorb of Mercaptopyridine molecule: a first principle study, J. Mol. Struct. 1205 (2020), 127593, https://doi.org/10.1016/j.molstruc.2019.127593.

[38] Y. Zhao, D.G. Truhlar, Exploring the limit of accuracy of the global hybrid meta density functional for main-group thermochemistry, kinetics, and noncovalent interactions, J. Chem. Theor. Comput. 4 (2008) 1849–1868, https://doi.org/10.1021/ct800246v.

[39] M.A.A. Ibrahim, Molecular mechanical perspective on halogen bonding, J. Mol. Model. 18 (2012) 4625–4638, https://doi.org/10.1007/s00894-012-1454-8.

[40] T. Lu, F. Chen Multiwfn, A multifunctional wavefunction analyzer, J. Comput. Chem. 33 (2012) 580–592, https://doi.org/10.1002/jcc.22885.

[41] R.M. Parrish, L.A. Burns, D.G.A. Smith, A.C. Simmonett, A.E. DePrince 3rd, E.G. Hohenstein, U. Bozkaya, A.Y. Sokolov, R. Di Remigio, R.M. Richard, et al., Psi4 1.1: an open-source electronic structure program emphasizing automation, advanced libraries, and interoperability, J. Chem. Theor. Comput. 13 (2017) 3185–3197, https://doi.org/10.1021/acs.jctc.7b00174.

[42] T.M. Parker, L.A. Burns, R.M. Parrish, A.G. Ryno, C.D. Sherrill, Levels of symmetry adapted perturbation theory (SAPT). I. Efficiency and performance for interaction energies, J. Chem. Phys. 140 (2014), 094106, https://doi.org/10.1063/1.4867135.
[43] V.N. Brudnyi, S.N. Grinyaev, V.E. Stepanov, Local neutrality conception - fermi-level pinning in defective semiconductors, Physica B 212 (1995) 429–435, https://doi.org/10.1016/0921-4526(95)00376-K.
[44] L.J. Sham, M. Schluter, Density-functional theory of the energy-gap, Phys. Rev. Lett. 51 (1983) 1888–1891, https://doi.org/10.1103/PhysRevLett.51.1888.
[45] R.D. Young, H.E. Clark, Effect of surface patch fields on field-emission work-function determinations, Phys. Rev. Lett. 17 (1966) 351, https://doi.org/10.1103/PhysRevLett.17.351.
[46] N.M. O'Boyle, A.L. Tenderholt, K.M. Langner cclib, A library for package-independent computational chemistry algorithms, J. Comput. Chem. 29 (2008) 839–845, https://doi.org/10.1002/jcc.20823.
[47] H. Zhu, C.F. Zhao, Q.H. Cai, X.M. Fu, F.R. Sheykhahmad, Adsorption behavior of 5-aminosalicylic acid drug on the B12N12, AlB11N12 and GaB11N12 nanoclusters: a comparative DFT study, Inorg. Chem. Commun. 114 (2020), 107808, https://doi.org/10.1016/j.inoche.2020.107808.
[48] M.J. Frisch, G.W. Trucks, H.B. Schlegel, G.E. Scuseria, M.A. Robb, J.R. Cheeseman, G. Scalmani, V. Barone, B. Mennucci, G.A. Petersson, et al., *Gaussian 09*, Revision E01; Gaussian09, Gaussian Inc., Wallingford CT, USA., 2009.
[49] W. Humphrey, A. Dalke, K. Schulten, VMD: visual molecular dynamics, J. Mol. Graph. 14 (1996) 33–38, https://doi.org/10.1016/0263-7855(96)00018-5.
[50] H. Karim, Shahnaz, M. Batool, M. Yaqub, M. Saleem, M.A. Gilani, S. Tabassum, A DFT investigation on theranostic potential of alkaline earth metal doped phosphorenes for ifosfamide anti-cancer drug, Appl. Surf. Sci. 596 (2022), 153618, https://doi.org/10.1016/j.apsusc.2022.153618.
[51] M. Kamel, M. Mohammadi, K. Mohammadifard, E.A. Mahmood, M.R. Poor Heravi, A. Heshmati, J.M, Z. Hossaini. Comprehensive theoretical prediction of the stability and electronic properties of hydroxyurea and carmustine drugs on pristine and Chitosan-functionalized graphitic carbon nitride in vacuum and aqueous environment, Vacuum 207 (2023), 111565, https://doi.org/10.1016/j.vacuum.2022.111565.
[52] D.H. Hassan, A.M. Rheima, M.M. Kadhim, H.A. Madlool, Z.M. Mahdi, M. Adel, S.K. Hachim, Adsorption behavior of carvedilol drug on delivery systems of pure aluminum nitrite nanotube and its Ni-doping and decorated from the theoretical perspective, Struct. Chem. (2023), https://doi.org/10.1007/s11224-023-02185-1.
[53] W. Kutzelnigg, Book review: atoms in molecules. A quantum theory. (International series monographs on chemistry, 22). By R. F. W. Bader. Angew. Chem. Int. Ed. Engl. 32 (1993) 128–129, https://doi.org/10.1002/anie.199301282.
[54] M.A. Alkhalifah, M. Yar, I. Bayach, N.S. Sheikh, K. Ayub, Covalent organic framework (C6N6) as a drug delivery platform for fluorouracil to treat cancerous cells: a DFT study, Materials 15 (2022) 7425, https://doi.org/10.3390/ma15217425.
[55] M. Perveen, S. Nazir, A.W. Arshad, M.I. Khan, M. Shamim, K. Ayub, M.A. Khan, J. Iqbal, Therapeutic potential of graphitic carbon nitride as a drug delivery system for cisplatin (anticancer drug): a DFT approach, Biophys. Chem. 267 (2020), 106461, https://doi.org/10.1016/j.bpc.2020.106461.
[56] A. Tariq, S. Nazir, A.W. Arshad, F. Nawaz, K. Ayub, J. Iqbal, DFT study of the therapeutic potential of phosphorene as a new drug-delivery system to treat cancer, RSC Adv. 9 (2019) 24325–24332, https://doi.org/10.1039/c9ra02778e.
[57] A. Allangawi, H. Sajid, K. Ayub, M.A. Gilani, M.S. Akhter, T. Mahmood, High drug carrying efficiency of boron-doped Triazine based covalent organic framework toward anti-cancer tegafur; a theoretical perspective, Comput. Theor. Chem. 1220 (2023), 113990, https://doi.org/10.1016/j.comptc.2022.113990.
[58] M. Asif, H. Sajid, K. Ayub, M.A. Gilani, N. Anwar, T. Mahmood, Therapeutic potential of oxo-triarylmethyl (oxTAM) as a targeted drug delivery system for nitrosourea and fluorouracil anticancer drugs; A first principles insight, J. Mol. Graph. Model. 122 (2023), 108469, https://doi.org/10.1016/j.jmgm.2023.108469.